A prototype high-resolution animal positron tomograph with avalanche photodiode arrays and LSO crystals

Sibylle I. Ziegler[1], Bernd J. Pichler[1], Guido Boening[2], Magdalena Rafecas[1], Wendelin Pimpl[2], Eckart Lorenz[2], Norbert Schmitz[2], Markus Schwaiger[1]

[1] Nuklearmedizinische Klinik und Poliklinik, Klinikum rechts der Isar der Technischen Universität München, Ismaninger Strasse 22, 81675 München, Germany
[2] Max-Planck-Institut für Physik, München, Germany

Received 25 August and in revised form 24 October 2000 / Published online: 14 December 2000

Abstract. To fully utilize positron emission tomography (PET) as a non-invasive tool for tissue characterization, dedicated instrumentation is being developed which is specially suited for imaging mice and rats. Semiconductor detectors, such as avalanche photodiodes (APDs), may offer an alternative to photomultiplier tubes for the readout of scintillation crystals. Since the scintillation characteristics of lutetium oxyorthosilicate (LSO) are well matched to APDs, the combination of LSO and APDs seems favourable, and the goal of this study was to build a positron tomograph with LSO-APD modules to prove the feasibility of such an approach. A prototype PET scanner based on APD readout of small, individual LSO crystals was developed for tracer studies in mice and rats. The tomograph consists of two sectors (86 mm distance), each comprising three LSO-APD modules, which can be rotated for the acquisition of complete projections. In each module, small LSO crystals (3.7×3.7×12 mm^3) are individually coupled to one channel within matrices containing 2×8 square APDs (2.6×2.6 mm^2 sensitive area per channel). The list-mode data are reconstructed with a penalized weighted least squares algorithm which includes the spatially dependent line spread function of the tomograph. Basic performance parameters were measured with phantoms and first experiments with rats and mice were conducted to introduce this methodology for biomedical imaging. The reconstructed field of view covers 68 mm, which is 80% of the total detector diameter. Image resolution was shown to be 2.4 mm within the whole reconstructed field of view. Using a lower energy threshold of 450 keV, the system sensitivity was 350 Hz/MBq for a line source in air in the centre of the field of view. In a water-filled cylinder of 4.6 cm diameter, the scatter fraction at the centre of the field of view was 16% (450 keV threshold). The count rate was linear up to 700 coincidence counts per second. In vivo studies of anaesthetized rats and mice showed the feasibility of in vivo imaging using this PET scanner. The first LSO-APD prototype tomograph has been successfully introduced for in vivo animal imaging. APD arrays in combination with LSO crystals offer new design possibilities for positron tomographs with finely granulated detector channels.

Keywords: Animal imaging – Positron emission tomography – Avalanche photodiodes – Instrumentation

Eur J Nucl Med (2001) 28:136–143
DOI 10.1007/s002590000438

Sibylle I. Ziegler (✉)
Nuklearmedizinische Klinik und Poliklinik,
Klinikum rechts der Isar der Technischen Universität München,
Ismaninger Strasse 22, 81675 München, Germany
e-mail: S.Ziegler@lrz.tu-muenchen.de
Tel.: +49-89-41404579, Fax: +49-89-41404841

Introduction

It has been recognized that the introduction of positron emission tomography (PET) scanning of mice and rats adds an important functional imaging modality to the biomedical laboratory [1, 2, 3]. Thus, high-resolution PET is increasingly used for non-invasive studies of small animals to image gene expression, treatment response or cardiac metabolism [4, 5, 6, 7].

While excellent spatial resolution is an obvious requirement for these systems, it is as important not to sacrifice sensitivity since specific activity of selective tracers may be limited [8]. Therefore, new technologies and detector designs have been introduced in this field, based either on traditional scintillator-block detectors or on new techniques for gamma ray or light detection [9, 10, 11, 12, 13]. While these systems are designed for animal studies, some of the principles can potentially also be transferred to larger tomographs and may also enhance clinical PET.

The detector components for coincidence imaging comprise scintillation crystals and light sensors. Lutetium oxyorthosilicate (LSO) [14] is the most promising scintillation material for improving PET detectors. LSO is fast and luminous, thus providing good timing and energy resolution. The microPET scanner was the first complete animal tomograph with LSO crystals [9, 15].

Detector performance is also influenced by the characteristics of the light sensor which detects the scintillation light. Traditionally, photomultiplier tubes (PMTs) are used. PMTs have been refined over a long period and provide excellent signal quality. Semiconductor detectors have the advantage of small size and mass production, but photodiodes without internal gain are not suitable for fast readout of low light levels. With the introduction of stable avalanche photodiodes (APDs), a semiconductor device with internal gain, new options for scintillation light detection became available. For PET requirements, it has been shown that APDs, especially in combination with LSO [16], yield results similar to PMTs. The group at Sherbrooke University pioneered the use of APDs and BGO crystals (bismuth germanate) in high-resolution PET [12, 17].

Spatial resolution in small-diameter tomographs with little effect of gamma-ray non-collinearity is mainly determined by the size of the scintillation crystals [18]. Small crystals, individually read out, proved to yield better resolution than block designs [19]. Block detectors, on the other hand, have the advantage of closely packed detector cells, a configuration which is otherwise difficult to achieve with PMTs and one-to-one coupling. Using position-sensitive photomultipliers and optical fibres as light guides, one solution to the problem of closely packing small crystals was realized in the microPET tomograph [9, 15].

Owing to their small size, APDs offer the potential of directly coupling scintillation crystals and light sensors. Two-dimensional arrays of APDs may further enhance the packing fraction of detector elements within a tomograph. The performance of commercial APDs has been improved considerably during the last few years [20, 21, 22, 23] and single-channel LSO-APD detectors for PET have been studied [16, 24, 25, 26, 27].

In this study, a prototype animal PET scanner with LSO-APD modules was developed and characterized. First in vivo studies in rats and mice were performed to show the feasibility of using LSO and APDs for high-performance PET.

Materials and methods

System description. MADPET (Munich Avalanche Diode PET) is a prototype positron tomograph which consists of six APD-LSO modules mounted on an octagonal support (Fig. 1). The detectors are grouped in two opposing segments of three modules each. The modules can be rotated by a computer-controlled stepping motor for step-and-shoot acquisitions of complete projections [25]. Each

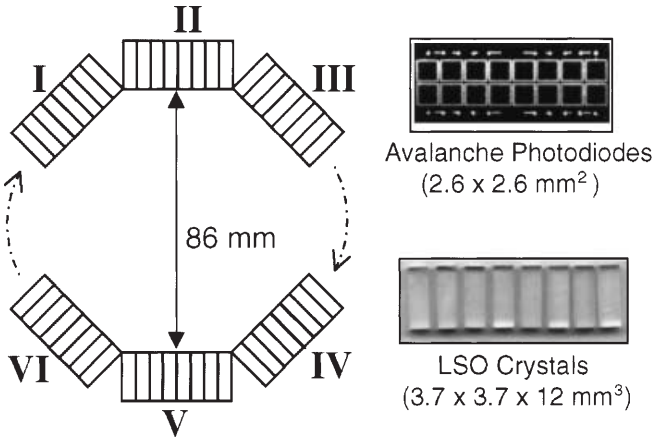

Fig. 1. Sketch of MADPET tomograph setup and detector modules. Six modules (I–VI), each containing one 2×8 APD matrix and LSO crystals, rotate around the object. List-mode data are collected during step-and-shoot acquisition of coincident events between the two detector sections

module contains two rows of eight LSO crystals (CTI Inc., Knoxville, Tenn., USA), which are arranged axially [26]. In this prototype, no axial side shielding is implemented. Since the number of available electronic channels is limited in the prototype scanner, only one layer of crystals is read out. The dimensions of the crystals are 3.7 mm×3.7 mm×12 mm, the distance between crystal centres being 4 mm. The space (0.3 mm) between the individual elements is filled with highly reflective material [28]. Opposite modules are 86 mm apart from each other. In each module, the crystals are individually coupled to one channel within matrices containing 2×8 square APDs (Hamamatsu Photonics, Hamamatsu City, Japan). Each APD has a sensitive area of 2.6×2.6 mm^2 and a capacitance of 50 pF. Stabilized high-voltage (EHQ F005, Iseg Rossendorf, Germany) of 300–400 V is used to bias the APDs such that the pulse heights are similar for all channels. The standard deviation of signal amplitudes for 511-keV gamma rays is less than 7.5%. At a gain of 100, these LSO-APD arrays showed an energy resolution of 14.7% at 511 keV [26] and a time resolution of 3.2 ns [26]. Because the APDs in the tomograph are operated at different gains ranging from 40 to 80, energy resolution varies between individual channels. The average energy resolution is 22% with a relative standard deviation of 10%. No drift in APD performance was noticed during continuous operation at room temperature (23°C).

To process the signals, fast charge sensitive preamplifiers (surface mount devices) are used which were specially developed for low noise performance (Max-Planck-Institut, München) [26]. Each signal is further amplified, split and fed into modular discriminators (discriminator 4413 LeCroy Corp., Chestnut Ridge, N.Y., USA), a coincidence unit (NIM logic unit 622 LeCroy Corp., Chestnut Ridge, N.Y., USA) and analogue-to-digital-converters (peak sensing ADC 2259B, LeCroy Corp., Chestnut Ridge, N.Y., USA). The discriminator levels are set above the noise level of the APDs. Whenever two discriminators (one in each segment) trigger within the coincidence timing window of 21 ns, all ADC channels are read out and the channel numbers and pulse heights are written to a file in sequence (list-mode acquisition). This is done for 30 angular steps covering 180°. After the first step, measurement time is increased for subsequent steps to compensate for radioactive decay. Data acquisition is accomplished by a PC

(AMD-K6, 350 MHz, Linux, 10 Mbit ethernet) with a CAMAC bus interface (Computer Automated Measurement And Control bus). Dead time due to CAMAC bus readout is measured online and the acquisition time per angular step is prolonged accordingly. Processing and reconstruction are performed by a separate PC (AMD-K6, 350 MHz, Linux, 10 Mbit ethernet). Both computers build a parallel virtual machine (PVM) to minimize interference of processing steps and acquisition handling. In addition to the computer readout, coincident count rates as well as random coincidence rates from a delayed coincidence circuit are monitored online using modular counters with a dwell time of 10 s.

A variable software threshold can be applied before reconstruction. Without rebinning, images are reconstructed directly from list-mode histograms using the iterative penalized weighted least squares (PWLS) algorithm [29] with 20 iterations. For this purpose, the detection probability matrix was extracted from Monte Carlo simulations of the whole tomograph [30]. Individual detector efficiencies were measured using a flat ^{18}F source and taken into account during reconstruction. The resulting image matrix consisted of 128×128 bins with a width of 1 mm per pixel.

In addition, filtered back-projection can be used to reconstruct sinograms after rebinning with bilinear interpolation (90 angular, 128 radial bins). Efficiency and sampling corrections are applied to the sinograms before reconstruction [31] by filtered back-projection.

Spatial resolution. The intrinsic resolution of the detector modules in coincidence was measured using a neutron-activated copper wire with a diameter of 0.6 mm (^{64}Cu activity: 7.5 MBq/cm). The tomograph was operated in stationary mode for this measurement. Starting from the centre of the tomograph, the line was suspended in air and stepped through the transaxial field of view in 0.5-mm increments. The measuring time at each position was 120 s. Data of each measurement were sorted according to lines of response perpendicular to the source movement. The coincidence counts of each pair of detectors above 450 keV within the central modules II and V were plotted versus the source position. From these curves, the intrinsic resolution of the system was determined as the full-width at half-maximum (FWHM) using linear interpolation.

Axial slice thickness was measured by stepping a horizontal line source through the axial field of view. The source consisted of an injection needle with a diameter of 0.9 mm, filled with aqueous solution of ^{18}F (180 MBq/ml). The needle covered 60 mm of the transaxial field of view. Images were acquired at 0.5-mm intervals. Axial count profiles at 0, 20 and 30 mm radial offset were generated from these data and the FWHM was determined in each profile.

Image resolution was determined from line source measurements. An injection needle with an inner diameter of 0.5 mm was filled with ^{18}F (1.4 MBq per centimetre) and positioned parallel to the tomograph axis in air. The line source was stepped through the field of view at intervals of 2 mm. For each position, a tomographic acquisition was performed over 180° with 30 steps of 2 s each. The coincidence data above 450 keV were reconstructed in a matrix of 128×128 pixels of 0.6 mm each, using the PWLS list-mode reconstruction. For comparison, the data were rebinned and reconstructed using a ramp filter (cut-off at the Nyquist frequency). Radial and tangential profiles through the resulting line source images were fitted with Gaussian functions.

Sensitivity. The sensitivity of the system was measured using the ^{64}Cu wire which was mentioned above. The wire was suspended in air at the centre of the tomograph, oriented along the tomograph axis. It covered the entire axial extent of the detector plane defined by the size of the LSO crystals (3.7 mm). Coincidence data above 450 keV were used to calculate system sensitivity.

Scatter fraction. The fraction of scattered events was estimated from measurements with a water cylinder (4.6 cm diameter, 5 cm length). A line source was inserted into the cylinder at the centre or 18 mm off axis. ^{18}F, mixed in water, was filled in the line source, the total activity being chosen to minimize random events to below 5% of the total rate. Coincidence data were sorted into sinograms (0.64-mm bins) applying an energy threshold of 450 keV. Similar to the procedure that is used in performance measurements of clinical tomographs, scattered events were identified in the sinogram as being registered more than twice the system resolution outside of the line source, corresponding to 8 pixels in this case. Linear interpolation was used under the peak of the line source. From this, scatter fraction was calculated as the number of events in the scatter region divided by the number of total counts.

Count rate performance. Since data in this prototype are acquired in list-mode applying a single hardware energy threshold, count rate performance of the system is limited by the total data rate on the CAMAC bus, regardless of the software threshold which can be applied during the list-mode sorting process. Thus, this measurement was performed with only one hardware discriminator setting, corresponding to the one used in further measurements. A lucite cylinder of 10 mm length and 35 mm diameter, filled with aqueous solution of 34 MBq ^{11}C, was positioned in the centre of the field of view. During decay of the ^{11}C activity, singles rates, random rates and total coincidence rates were monitored for a duration of 2 h. Every 1–2 min, an acquisition of 30 s (10 s within the first 17 min) was started for the measurement of total acquired coincidence data.

In addition, a measurement with a lucite cylinder of 5 cm length and 4.6 cm diameter, filled with aqueous solution of ^{18}F (39 MBq), was performed. The cylinder was positioned in the centre of the field of view and singles rates as well as coincidence events were monitored for 3 h. This geometry was chosen to resemble the “worst case” in animal studies with an extended activity distribution outside the coincidence field of view.

In vivo studies. First in vivo studies of anaesthetized rats and mice were performed. Animal experiments were conducted according to the rules of our institution and the law on the protection of animals. After anaesthetizing the animals, the radioactive tracer was injected via the tail vein. The amount of injected activity was determined by the count rate limitations of the system and by the amount of substance which could be used in the small animals, depending on the specific activity. After a waiting period, the length of which depended on the uptake kinetics of the tracer used, the animals were positioned in the tomograph and data acquisition was initiated. Each slice was acquired with 30 steps over 180°. To cover larger volumes, several acquisitions with 2-mm axial offset were carried out. The list-mode data were reconstructed with the PWLS algorithm (20 iterations, smoothing factor 19), applying a lower energy threshold of 450 keV. No correction of attenuation was performed in these studies.

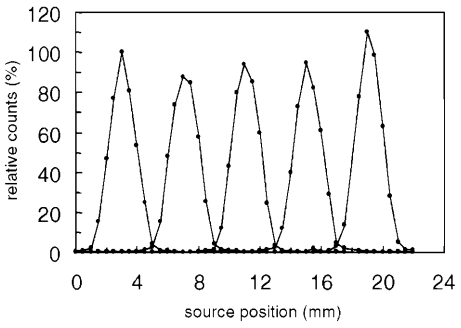

Fig. 2. Intrinsic resolution, measured using a line source moving horizontally through the tomograph across modules II and V. Plotted are the counts for five opposing detector pairs

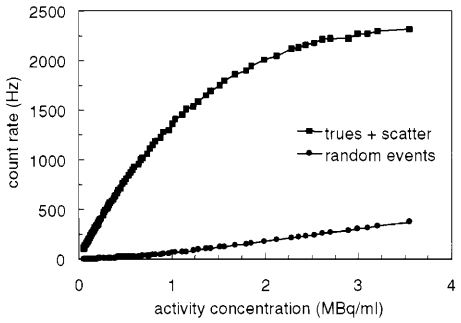

Fig. 4. Count rate performance measured with a short cylinder, filled with ^{11}C. *Squares* are the count rates of true and scattered events, *circles* are the count rates of random events as a function of activity concentration in the phantom (3.5 cm diameter, 10 mm length)

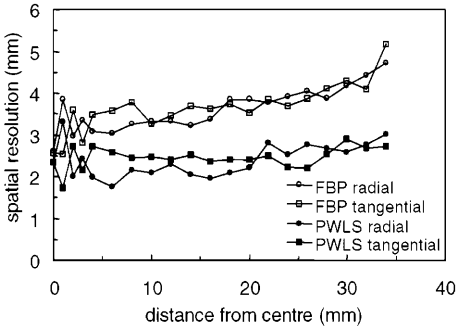

Fig. 3. Reconstructed resolution (FWHM) in radial (*circles*) and tangential (*squares*) directions in the images of line sources. PWLS list-mode reconstruction (*solid symbols*) including the probability weights from Monte Carlo simulations of the whole system is compared with rebinning and filtered back-projection (*open symbols*) using a Ramp filter with the cut-off at the Nyquist frequency

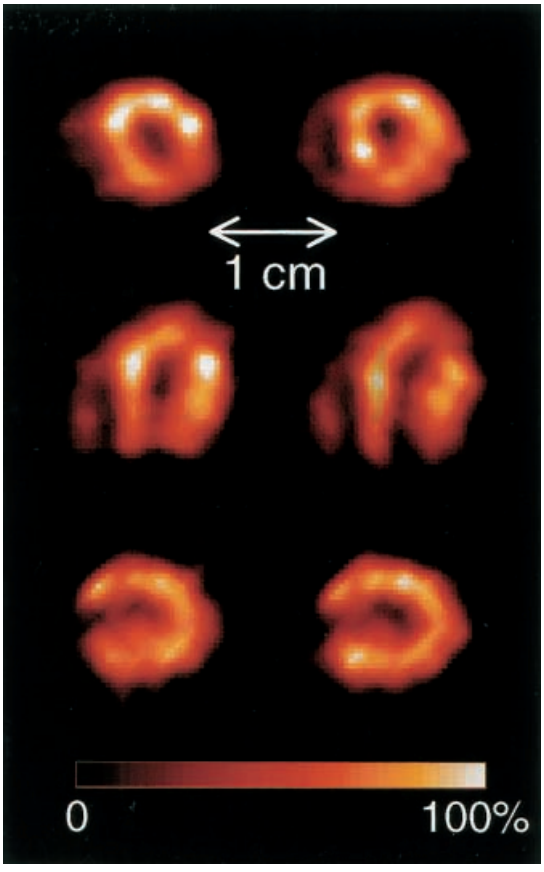

Fig. 5. In vivo scan of FDG distribution in a normal rat heart (40 min after injection of 37 MBq ^{18}F-FDG). Volume data were acquired slice after slice by stepping the animal in supine position through the tomograph. Two short-axis, horizontal and vertical long-axis slices are shown

Results

Spatial resolution

Using the copper line source, coincidence count rate was 203 Hz in the centre of the field of view and the random fraction was 1.3%. The average intrinsic spatial resolution was 2.1±0.1 mm in the central modules II and V (Fig. 2).

Axial slice thickness was 1.9 mm at the centre of the field of view, and 2.3 mm (2.6 mm) at 20 mm (30 mm) off-centre.

Radial and tangential profiles in the images of line sources from list-mode PWLS reconstruction (filtered back-projection) showed a reconstructed resolution (FWHM) of 2.3 mm (2.6 mm) in the centre and 2.3 mm (3.5 mm) in a 14 mm off-centre position. Radial resolution did not differ from tangential values. Figure 3 shows that changes in spatial resolution are minimized if the system response model is taken into account during list-mode PWLS reconstruction.

Sensitivity

The measured coincidence rate was 350 counts per second per 1 MBq of pure positron emitter. This translates into a sensitivity of 95 Hz/MBq per axial millimetre.

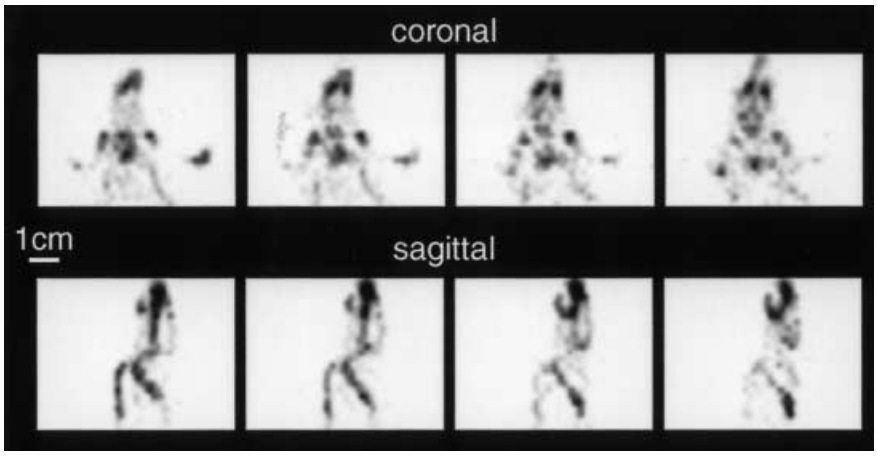

Fig. 6. In vivo scan of $^{18}F^-$ uptake in a mouse skeleton. The mouse (41 g) was positioned supine in the tomograph. Acquisition started 30 min after injection of 22 MBq $^{18}F^-$. Data from 25 transaxial planes were reoriented in coronal and sagittal slices

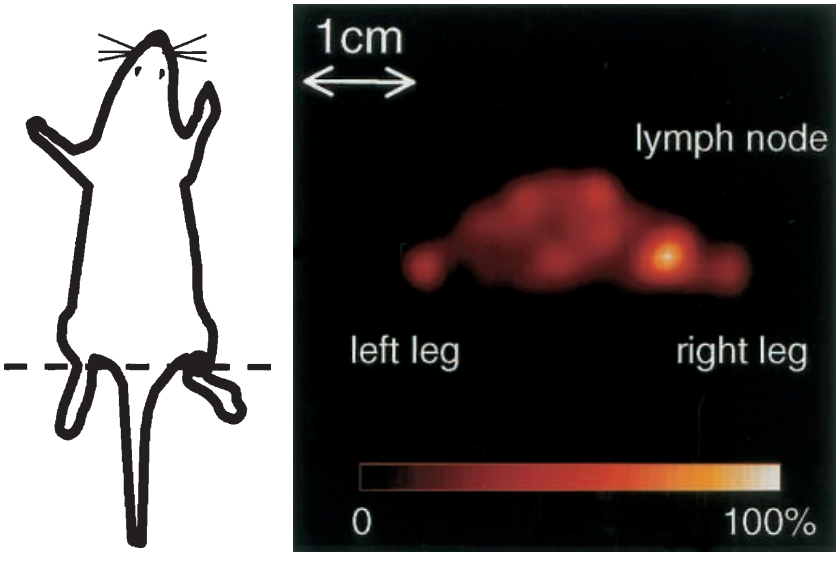

Fig. 7. In vivo imaging of amino acid uptake in a tumour-infiltrated lymph node of a mouse. The mouse was scanned in the prone position. Acquisition started 90 min after injection of 24 MBq ^{18}F-FET. The measuring time was 90 s

Scatter fraction

The scatter fraction in water was 16% in the centre and 17% at the 18 mm off-centre position.

Count rate performance

In Fig. 4, the random count rate and the random corrected coincidence count rate are plotted versus activity concentration in the test source. The coincidence count rate was linear up to 700 Hz, corresponding to 4.1 MBq total activity in the small cylinder phantom. At higher activity levels, dead time effects were noticeable. Dead time losses could be described by a paralysable model with a dead time constant of 0.16 ms.

Since most of the activity was contained within the field of view, random events reached a maximum of only 15% at a total activity of 34 MBq in the small phantom. For the large cylinder, random contribution was significantly higher owing to the activity outside of the field of view. In this case, random events amounted to 50% of the total count rate at an activity concentration of 470 kBq/ml, corresponding to a total of 39 MBq in the phantom.

In vivo studies

Seven transaxial slices through the heart of a rat (500 g) were acquired 40 min after injection of 37 MBq ^{18}F-fluorodeoxyglucose (FDG). Total acquisition time of all slices was 18 min. Figure 5 shows examples of the reoriented short-axis and long-axis slices.

The skeleton of a mouse (41 g) was studied after injection of 22 MBq $^{18}F^-$. Measurements started 30 min after injection. Twenty-five consecutive transaxial slices were acquired, covering the region from head to lower ribs. Coronal and sagittal views of the $^{18}F^-$ uptake in the mouse bones are shown in Fig. 6.

Amino acid uptake in lymph nodes infiltrated with tumour cells was studied in mice using ^{18}F-labelled fluoroethyl-L-tyrosine (FET). A series of transaxial slices (2 mm separation) was acquired for 90 s each, starting

90 min after injection of the tracer (24 MBq). Figure 7 is a transaxial image through the region of the lymph node. Enhanced FET uptake is clearly seen in the tumour-infiltrated lymph node on the right leg, whereas no increased uptake can be seen in the contralateral lymph node.

Discussion

The prototype animal PET scanner MADPET is the first tomograph which employs LSO and APDs. Close packing of LSO crystals was achieved by the introduction of APD arrays. While the main purpose of building MADPET was the proof of principle, the tomograph can already function as an imaging device and is being used in our department for non-invasive tracer distribution studies in radiochemistry and oncological research.

The tomograph can acquire a single transaxial image with a slice thickness of 2 mm and a transaxial image resolution of 2.4 mm.

There is only one other APD tomograph in operation, the BGO-APD tomograph which was developed at the University of Sherbrooke [12, 32]. In contrast to this scanner, MADPET combines matrices of APDs with individual crystals in the front-end detector modules. In addition to the improved APD characteristics, MADPET also shows that APDs are well matched to the scintillation properties of LSO. The APD arrays used in our prototype proved to be very stable over a long period of operation (months). Compared to the results with BGO [12], energy resolution of MADPET is 70% better. Owing to the fast decay time of LSO, timing resolution can potentially be in the order of 3 ns, compared with 12 ns in the case of BGO-APD modules [12], although a wider window is used in the MADPET prototype because of restrictions in the modular readout electronics. Despite the fact that the crystals are only half as long, owing to the much smaller diameter, sensitivity per millimetre axial extent of the sector tomograph MADPET is only about a factor of 3 lower than that of the whole ring Sherbrooke tomograph when the typical energy thresholds are applied.

The intrinsic spatial resolution of MADPET is limited by the crystal size and is larger than in some other small animal scanners [13, 15] but about half of the resolution which can be achieved with high-resolution clinical scanners [33]. Compared with the existing BGO-APD tomograph [12], the transaxial resolution is similar (2.4 mm vs 2.1–3.0 mm) and the axial resolution is slightly better because of the smaller crystals in MADPET (2 mm vs 3.1 mm in the centre). Imaging in mice will benefit from further improving the spatial resolution. This will be addressed in a new design of a complete LSO-APD positron tomograph.

Using an iterative reconstruction algorithm which implements the device-specific spatially dependent line spread function, the reconstructed field of view could be extended to 80% of the detector diameter with a spatial resolution similar to the intrinsic resolution of the modules. Figure 3 clearly demonstrates the improved resolution of list-mode reconstruction in terms of homogeneity and absolute value, as compared with rebinning and filtered back-projection. Resolution recovery is essential for small-diameter tomographs, and other approaches are possible, e.g. sinogram restoration [34]. In our study we developed a method which uses the advantages of statistical reconstruction and the known line spread functions.

A major limitation of MADPET is its low sensitivity. There are several reasons for this: The solid angle of the detector system is small because only one detector plane is operated and only 6/8 of a ring is covered. Furthermore, due to the inherent variability of the APD gains it was necessary to choose a high energy threshold (450 keV) in order to eliminate noise contributions from the APDs. This will be improved by the next generation of low-noise APDs (Hamamatsu Photonics, Japan).

In terms of sensitivity per axial extent, MADPET has almost four times less sensitivity per millimetre than the microPET tomograph [15], but it is similar to other crystal-based tomographs with limited angular coverage [13] and has twice the sensitivity per millimetre of the HIDAC system [10], which does not use scintillation crystals. The reason for this comparatively high sensitivity is the relatively large LSO volume in MADPET. Extending the axial field of view by adding more detector rings and 3D data acquisition would be straightforward and was not considered in this feasibility study.

The count rate characteristics of this system show a long dead-time. This is entirely caused by the computer readout interface, which was not optimized for this purpose. Instead, a general, low-cost system was chosen. A dedicated system with faster read and write access will greatly enhance the performance.

The preliminary in vivo scans demonstrate the usefulness of MADPET for non-invasive biodistribution studies. Dynamic scans of frame lengths less than 1 min are not possible since the tomograph needs to be rotated. A step number of 30 was chosen in order to achieve adequate sampling [31]. Reducing the number of angular steps could offer the option of shorter total acquisition time in cases where spatial resolution is not of utmost importance.

Quantification will require proper attenuation correction. While no transmission measurement is performed on the current system, the calculation of attenuation factors from CT data seems to be most favourable and is being considered for future designs. Further research will also be devoted to implementing adequate scatter correction methodology.

Optimizing the LSO-APD detector concept with regard to higher resolution and sensitivity is feasible and under way. New APD arrays with smaller pixels and lower noise have been developed which will facilitate the readout of smaller LSO crystals. With a novel dual-layer module depth-of-interaction information will be

gained and a spatial resolution of less than 2 mm is anticipated in a ring tomograph. The increase in solid angle and in sensitive volume will result in a six times higher sensitivity than is achieved with the current MADPET system operated at a 450-keV energy threshold. At a 100-keV threshold, the expected sensitivity will be almost 30 times higher than with MADPET.

Future work includes the development of dedicated, integrated electronics as well as the investigation of reconstruction methodology including information from two detector layers.

In conclusion, the first prototype tomograph built with small LSO crystals and APD arrays is operational and has proved to be suitable for in vivo animal studies in rats and mice. Advantages of using APDs in PET include their compactness, high quantum efficiency, low noise, suitability for detector arrays and low production cost. Adaptation of this detector concept to larger scale tomographs seems feasible.

Acknowledgements. The MADPET team thanks the members of the electronics group and the mechanical workshops at the Max-Planck-Institut für Physik for their professional work and helpful discussions during the development of the prototype scanner. We thank the staff of the cyclotron and radiochemistry group at the Nuklearmedizinische Klinik rechts der Isar for reliable delivery of tracers. Special thanks go to N. Nguyen for her excellent help in performing the in vivo animal studies. The authors thank Dr. Yamamoto (Hamamatsu Photonics) for his interest in this work and his support in the development of APD arrays. The help and advice of Dr. R. Nutt, Dr. C. Melcher and Dr. M. Casey (CTI Inc.) is gratefully acknowledged.

This study was supported by grants from the Deutsche Forschungsgemeinschaft (DFG Zi 615/1-1) and from the European Union (FMBICT972797).

References

1. Phelps ME. PET: the merging of biology and imaging into molecular imaging. *J Nucl Med* 2000; 41:661–681.
2. Tornai MP, Jaszczak RJ, Turkington TG, Coleman RE. Small-animal PET: advent of a new era of PET research. *J Nucl Med* 1999; 40:1176–1179.
3. Hume S, Jones T. Positron emission tomography (PET) methodology for small animals and its application in radiopharmaceutical preclinical investigation. *Nucl Med Biol* 1998; 25: 729–732.
4. Gambhir SS, Barrio JR, Wu L, Iyer M, Namavari M, Satyamurthy N, Bauer E, Parrish C, MacLaren DC, Borghei AR, Green LA, Sharfstein J, Berk AJ, Cherry SR, Phelps M, Herschman HR. Imaging of adenoviral-directed herpes simplex virus type 1 thymidine kinase reporter gene expression in mice with radiolabeled ganciclovir. *J Nucl Med* 1998; 39: 2003–2011.
5. Lapointe D, Brasseur N, Cadorette J, La Madeleine C, Rodrigue S, van Lier JE, Lecomte R. High-resolution PET imaging for in vivo monitoring of tumor response after photodynamic therapy in mice. *J Nucl Med* 1999; 40:876–882.
6. Moore JV, Waller ML, Zhao S, Dodd NJF, Acton PD, Jeavons AP, Hastings DL. Feasibility of imaging photodynamic injury to tumours by high-resolution positron emission tomography. *Eur J Nucl Med* 1998; 25:1248–1254.
7. Kornblum HI, Araujo DM, Annala AJ, Tatsukawa KJ, Phelps ME, Cherry SR. In vivo imaging of neuronal activation and plasticity in the rat brain by high resolution positron emission tomography (microPET). *Nat Biotechnol* 2000; 18:655–660.
8. Hume SP, Gunn RN, Jones T. Pharmacological constraints associated with positron emission tomographic scanning of small laboratory animals. *Eur J Nucl Med* 1998; 25:173–176.
9. Cherry S, Shao Y, Silverman R, Meadors K, Siegel S, Chatziioannou A, Young J, Jones W, Moyers J, Newport D, Boutefnouchet A, Farquhar T, Andreaco M, Paulus M, Binkley D, Nutt R, Phelps M. MicroPET: a high resolution PET scanner for imaging small animals. *IEEE Trans Nucl Sci* 1997; 44:1161–1166.
10. Jeavons AP, Chandler RA, Dettmar CAR. A 3D HIDAC-PET camera with sub-millimetre resolution for imaging small animals. *IEEE Trans Nucl Sci* 1999; 46:468–473.
11. Bruyndonckx P, Liu X, Tavernier S, Shuping Z. Performance study of a 3D small animal PET scanner based on BaF_2 crystals and photo sensitive wire chambers. *Nucl Instr Meth* 1997; A 392:407–413.
12. Lecomte R, Cadorette J, Rodrigue S, Lapointe D, Rouleau D, Bentourkia M, Yao R, Msaki P. Initial results from the Sherbrooke avalanche photodiode positron tomograph. *IEEE Trans Nucl Sci* 1996; 43:1952–1957.
13. Weber S, Herzog H, Cremer M, Engels R, Hamacher K, Kehren F, Muehlensiepen H, Ploux L, Reinartz R, Reinhart P, Rongen F, Sonnenberg F, Coenen HH, Halling H. Evaluation of the TierPET system. *IEEE Trans Nucl Sci* 1999; 46:1177–1183.
14. Melcher C, Schweitzer J. Cerium-doped lutetium oxyorthosilicate: a fast, efficient new scintillator. *IEEE Trans Nucl Sci* 1992; 39:502–505.
15. Chatziioannou AF, Cherry SR, Shao Y, Silverman RW, Meadors K, Farquhar TH, Pedarsani M, Phelps ME. Performance evaluation of microPET: a high-resolution lutetium oxyorthosilicate PET scanner for animal imaging. *J Nucl Med* 1999; 40:1164–1175.
16. Schmelz C, Bradbury SM, Holl I, Lorenz E, Renker D, Ziegler S. Feasibility study of avalanche photodiode readout for a high resolution PET with nsec time resolution. *IEEE Trans Nucl Sci* 1995; 42:1080–1084.
17. Lecomte R, Cadorette J, Richard P, Rodrigue S, Rouleau D. Design and engineering aspects of a high resolution positron tomograph for small animal imaging. *IEEE Trans Nucl Sci* 1994; 41:1446–1452.
18. Levin CS, Hoffman EJ. Calculation of positron range and its effect on the fundamental limit of positron emission tomography system spatial resolution. *Phys Med Biol* 1999; 44:781–799.
19. Moses WW, Derenzo SE. Empirical observation of resolution degradation in positron emission tomography utilizing block detectors. *J Nucl Med* 1993; 34:101P.
20. Lorenz E, Natkaniec S, Renker D, Schwartz B. Fast readout of plastic and crystal scintillators by avalanche photodiodes. *Nucl Instr Meth* 1994; A344:64–72.
21. Holl I, Lorenz E, Natkaniec S, Renker D, Schmelz C, Schwartz B. Some studies of avalanche photodiode readout of fast scintillators. *IEEE Trans Nucl Sci* 1995; 42:351–356.
22. Moszynski M, Ludziejewski T, Wolski D, Klamra W, Szawlowski M, Kapusta M. Subnanosecond timing with large area avalanche photodiodes. *IEEE Trans Nucl Sci* 1996; 43: 1298–1302.

23. Moszynski M, Kapusta M, Wolski D, Szawlowski M, Klamra W. Blue enhanced large area avalanche photodiodes in scintillation detection with LSO, YAP and LuAP crystals. *IEEE Trans Nucl Sci* 1997; 44:436–442.
24. Ziegler SI, Schmelz C, Lorenz E, Renker D. Avalanche photodiode readout of lutetium-oxyortho-silicate for high resolution positron emission tomography. In: Dorenbos O, vanEijk CWE, eds. *SCINT95*. Delft University Press, 1995.
25. Fries O, Bradbury SM, Gebauer J, Holl I, Lorenz E, Renker D, Ziegler SI. A small animal PET prototype based on LSO crystals read out by avalanche photodiodes. *Nucl Instr Meth* 1997; A387:220–224.
26. Pichler B, Boening G, Lorenz E, Mirzoyan R, Pimpl W, Schwaiger M, Ziegler SI. Studies with a prototype high resolution PET scanner based on LSO-APD modules. *IEEE Trans Nucl Sci* 1998; 45:1298–1302.
27. Lecomte R, Pepin C, Rouleau D, Saoudi A, Andreaco M, Casey M, Nutt R, Dautet H, Webb P. Investigation of GSO, LSO and YSO scintillators using reverse avalanche photodiodes. *IEEE Trans Nucl Sci* 1998; 45:478–482.
28. Pichler BJ, Lorenz E, Mirzoyan R, Weiss L, Ziegler SI. Production of a diffuse very high reflectivity material for light collection in nuclear detectors. *Nucl Instr Meth* 2000; A442:333–336.
29. Fessler JA. Penalized weighted least squares image reconstruction for positron emission tomography. *IEEE Trans Med Imag* 1994; 13:290–300.
30. Boening G, Pichler BJ, Rafecas M, Schwaiger M, Lorenz E, Ziegler SI. Improved image generation for high resolution animal PET using Monte-Carlo simulations of the system response function. *J Nucl Med* 2000; 41:196P.
31. Rafecas M, Boening G, Pichler BJ, Lorenz E, Schwaiger M, Ziegler SI. Compensation for geometric effects and normalization in a high resolution animal PET scanner. *Eur J Nucl Med* 1999; 26:1029.
32. Marriot CJ, Cadorette JE, Lecomte R, Scasnar V, Rousseau J, vanLier JE. High-resolution PET imaging and quantitation of pharmaceutical biodistributions in a small animal using avalanche photodiode detectors. *J Nucl Med* 1994; 35:1390–1396.
33. Brix G, Zaers J, Adam LE, Bellemann ME, Ostertag H, Trojan H, Haberkorn U, Doll J, Oberdorfer F, Lorenz WJ. Performance evaluation of a whole-body PET scanner using the NEMA protocol. *J Nucl Med* 1997; 38:1614–1623.
34. Kao CM, Pan X, Chen CT. Accurate image reconstruction using DOI information and its implications for the development of compact PET systems. *IEEE Trans Nucl Sci* 2000; 47: 1551–1560.